Laser & Photonics Reviews

LASER & PHOTONICS REVIEWS

www.lpr-journal.org

RESEARCH ARTICLE OPEN ACCESS

Extreme Optical Field Confinement and Enhancement in a Plasmonic Picopatch Within a Nanoparticle-on-Mirror Resonator

Jinna He[1,2] | Mario Zapata-Herrera[2,3] | Xabier Arrieta[2,4] | Mingli Wan[1] | Yuan Zhang[5,6] | Javier Aizpurua[3,4,7] | Ruben Esteban[2,3]

[1]School of Electric and Mechanical Engineering, Pingdingshan University, Pingdingshan, China | [2]Centro de Física de Materiales (CFM-MPC), CSIC-EHU, Paseo Manuel de Lardizabal 5, San Sebastián, Spain | [3]Donostia International Physics Center (DIPC), Paseo Manuel de Lardizabal 4, San Sebastián, Spain | [4]Dpt. of Electricity and Electronics, University of the Basque Country (EHU), Leioa, Spain | [5]Henan Key Laboratory of Diamond Materials and Devices, Key Laboratory of Material Physics, Ministry of Education, School of Physics, Zhengzhou University, Zhengzhou, China | [6]Institute of Quantum Materials and Physics, Henan Academy of Sciences, Zhengzhou, China | [7]Ikerbasque, Basque Foundation for Science, María Díaz de Haro 3, Bilbao, Spain

Correspondence: Ruben Esteban (ruben.esteban@ehu.eus)

Received: 25 February 2026 | **Revised:** 22 May 2026 | **Accepted:** 22 June 2026

ABSTRACT

Plasmonic resonances in metallic nanogaps can confine light into nanometric regions, but reaching modes of volume ≈ 1 nm^3 remains challenging. We present a detailed theoretical analysis of the optical modes of an experimentally-motivated nanoresonator configuration that contains a picopatch formed by the lifting of a few gold atoms in the gap of a Nanoparticle-on-Mirror (NPoM) structure. Classical simulations indicate that the plasmonic modes associated with the picopatch geometry can confine light to extremely small regions and are highly sensitive to the picopatch size and shape, enabling broad tunability. Furthermore, these modes can couple strongly with other nanocavity modes of the structure, as identified from a clear anti-crossing behavior of the polaritonic resonances. Remarkably, up to $\approx$ 2000-fold electric field enhancement inside the picopatch and tiny effective mode volumes approaching ≈ 1 nm^3 are obtained. Further, changing the morphology of the picopatch does not modify the qualitative findings, and increasing the absorption losses in the classical simulations, to mimic quantum (non-local) effects in the metal permittivity, decreases the electric field enhancement only moderately. Compared to the standard picocavities formed by single-atom protrusions, picopatches are an intriguing alternative to reach extreme optical field confinement and enhancement in plasmonic cavities.

1 | Introduction

Optical modes can confine light to small regions and are very attractive to miniaturize optical devices and simultaneously increase light-matter interaction. Notably, localized surface plasmons induced by the hybridization of optical fields and collective electronic excitations in metallic nanoparticles enable strong absorption and scattering of light, as well as light confinement well below the diffraction limit [1, 2]. The plasmonic properties of these metallic nanoparticles can be altered by changing their geometry [3], and thus a variety of metallic (plasmonic) nanostructures, from single nanoparticles of various geometries [4–7] to complex arrangements of multiple building blocks [8–10], have been widely explored in recent years to achieve optimized field confinement and enhancement, for example [11]. In this context, a canonical configuration is the NanoParticle-on-Mirror (NPoM) optical resonator [12–15], which can confine light very efficiently into the gap that separates a metallic nanoparticle from a metallic substrate (the mirror). An exquisitely defined NPoM gap thickness down to less than 1 nm [16], typically set by a molecular

monolayer or two-dimensional material that serves as a spacer, leads to several-hundred-fold electric field enhancements in the gap. The effective mode volume in the gaps of NPoM structures is tens to hundreds of cubic nanometers, about 6–7 orders of magnitude below the diffraction limit [17], making the NPoM geometry a robust platform for a wide range of applications including Surface-Enhanced Raman or Fluorescence Spectroscopy (SERS and SEFS), nonlinear optics, plasmonic sensing, plasmon-exciton ultra-strong coupling, optoelectronic devices, optomechanics and quantum optics [15, 18].

Plasmonic resonances in the NPoM structures with ultrathin nanogaps are very sensitive to the precise structural details of the gap [19–21]. Notably, it has been demonstrated that atomic protrusions in these gaps can localize electromagnetic fields into regions ('hot spots') down to sub-nanometric dimensions ('picocavities') [22–27]. Similar effects due to the presence of picocavities in a tip can be also clearly observed in scanning tunneling microscopy (STM) experiments that demonstrate spectral imaging with spatial resolution below 1 nm [28–30]. However, although the volume of the hot spot in these 'picocavities' is often smaller than 1 nm^3, the volume of the electromagnetic mode in a quantum-mechanical picture (see definition of this volume below) can be much larger, except for very specific configurations, such as those studied in Refs. [26, 31].

Picocavities are spontaneously formed in NPoM resonators by random motions of single (or very few) surface metallic atoms under intense laser illuminations, as sketched in Figure 1a. These motions could be induced by the thermal energy or optical forces. On the other hand, ultra-high-vacuum transmission electron microscopy (TEM) experiments [32] have also observed the collective delamination of several metallic atoms (e.g., patches of 5–10 atoms wide), which forms a tiny (subatomic thick and nanometer wide) empty slot between them and the metallic surface (Figure 1b). Here we call these structures 'picopatches', even if their lateral dimensions can be slightly larger than 1 nm, in analogy to the picocavities formed by isolated atomic protrusions. Our previous work [33] suggested that the formation of picopatches in the NPoM nanoresonators (Figure 1c) can be behind experimental observations of transient and spectrally broad emission (flares) from plasmonic nanostructures [34–36], due to strong localization and enhancement of the fields. However, this previous work was focused on the analysis of the laterally infinite metal-insulator-metal-insulator (MIMI) planar waveguide systems, with only preliminary simulations of a full 3-dimensional NPoM resonator with a picopatch.

In this work, we show the potential of a NPoM containing a picopatch as an extreme field confiner in realistic configurations (Figure 1c), through a detailed theoretical analysis of their optical properties. We first discuss the existence of the plasmonic modes associated with the picopatch and characterize their properties based on calculations of a planar MIMI configuration. We then analyze the optical response of the full NPoM system depicted in Figure 1c, focusing on the extreme field enhancement and confinement that can be reached. We also analyze the tunability of the modes in this structure with modifications of the structural parameters as well as the emergence of hybrid modes due to the strong coupling between the modes confined in the picopatch and other modes confined in the NPoM nanocavity. The coupling strength that characterizes this interaction is extracted from a coupled harmonic oscillator model, and the mode volume of the hybrid modes is evaluated to quantify the extreme, close to 1 nm^3, field confinement. Last, we examine the robustness of the results by considering modifications of the exact picopatch configuration and of the absorption losses. These modifications are motivated by the impossibility of knowing or controlling the precise experimental geometry, and by the fact that the local classical permittivity used in the simulations becomes less well justified at tiny scales due to quantum (non-local) effects.

2 | Morphology

The configuration of the NPoM resonator containing the picopatch is shown schematically in Figure 1c, with the zoom on the right focusing on the structural details of the picopatch itself. A bare NPoM resonator (corresponding to the same geometry but without the picopatch) is used as a reference and consists of a truncated Au spherical nanoparticle of radius $r_{sphere} = 40$ nm with a flat bottom facet of radius $r_{facet} = 30$ nm separated from a semi-infinite Au substrate underneath by a dielectric spacer of thickness $d = 1.1$ nm and permittivity $\varepsilon_{d1} = 2.1$ (all values given in this section are those used in the calculations except when explicitly mentioned otherwise). The spacer covers the whole Au substrate and can represent a molecular monolayer, for example. Inside the NPoM gap, the picopatch is formed by a few Au atoms that are lifted from the bottom metallic substrate, so that they are separated $\delta = 0.2$ nm from it. These lifted atoms are placed below the center of the flat facet and present a circular cross section in the horizontal x-y plane parallel to the Au substrate. The thickness of the lifted Au atoms is set to be $t = 0.235$ nm and corresponds to the thickness of an Au monolayer (as set by the Au (111) layer spacing). The slot between the Au monolayer and the underlying bulk Au is filled up by vacuum with permittivity $\varepsilon_{d2} = 1.0$. The slot has a typical radius $r_{slot} = 1.435$ nm, corresponding to a lateral width of ~ 10 Au atoms. The picopatch corners are rounded to avoid unphysical divergences in the classical calculations of field enhancements. The whole structure is rotationally symmetric and is illuminated by a plane wave incoming with an incidence angle of 45^0 with respect to the normal of the substrate (z-axis) and polarized in the x-z plane of incidence (p-polarization) (see the axis of coordinates, illumination and details of the geometry in the sketches in Figure 1c).

3 | Methodology

The classical optical response of the NPoM resonator that contains the picopatch is obtained using full-wave simulations implemented in COMSOL Multiphysics [37]. The computational model contains the structure under consideration, and the sphere-shaped perfectly matched layers (PML) that are applied in all directions to eliminate nonphysical boundary reflections. Since the structure involves a semi-infinite gold substrate, an analytical background field instead of a plane wave is used as an excitation [38]. This background field corresponds to that excited by a plane wave in a layered system formed by the gold substrate, the $d = 1.1$ nm thick dielectric layer and the vacuum on top. The permittivity of gold ε_{Au} is taken from experimental data [39], except when stated otherwise. The scattering cross section

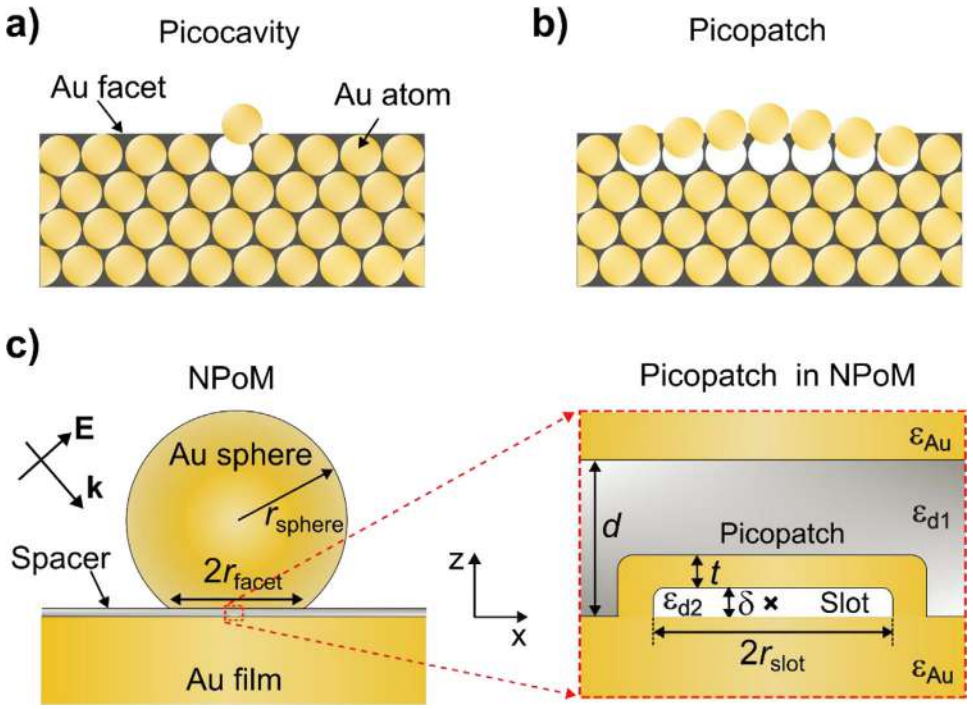

FIGURE 1 | NPoM resonator with picopatch. (a, b) Schematics of an Au interface, showing (a) a single adatom protruding from the surface (picocavity) and (b) delamination of a few atoms in the top Au monolayer (picopatch). White circles represent the original position of the gold atoms before they move to form the picocavity or picopatch. (c) Sketch of the NPoM resonator with a picopatch considered in this work, with the zoom on the right focusing on the structural details of the picopatch itself. The NPoM consists of a truncated Au nanosphere of radius $r_{sphere} = 40$ nm over a semi-infinite Au substrate, with a $d = 1.1$ nm thick dielectric spacer of permittivity $\varepsilon_{d1} = 2.1$ between them forming a nanogap that contains the picopatch. The truncated Au sphere presents a circular flat facet at the bottom of radius $r_{facet} = 30$ nm, which corresponds to the upper interface of the nanogap. The picopatch is situated in the nanogap, below the center of the flat facet, and it consists of a small circular section of an Au monolayer (thickness $t = 0.235$ nm and radius r_{slot}), at a $\delta = 0.2$ nm distance from the underlying substrate, leaving a vacuum slot in the middle (permittivity $\varepsilon_{d2} = 1.0$). A vertical wall of the same thickness t connects the edges of the monolayer and the substrate (see zoom in the right panel for details). The full geometry is rotationally symmetric around the vertical z-direction, and the illumination is a p-polarized wave incoming in the x-z plane at a 45^0 angle with respect to the vertical z direction (x and z directions are indicated in (c), with the nanogap center corresponding to x = y = 0 and z = 0.55 nm). The black cross at the center of the slot (x = y = 0 and z = 0.1 nm) indicates the position where the electric fields are often evaluated and where a dipole is placed when calculating the Purcell factor in the main text.

is obtained by computing the surface integral of the scattered Poynting vector in the upper semi-sphere at the internal boundary of the PML layer. The absorption cross section is obtained by calculating the volume integral of the resistive losses in the metallic regions occupied by the gold nanosphere and the lifted gold monolayer. Note that we do not extend this integral to the metallic substrate, so that the absorption obtained is smaller than if the substrate were included. This simplification should not affect the spectral shape and thus the identification and analysis of the modes. Considering the extremely small dimensions of the picopatch, the convergence of the calculations was carefully verified by varying the size of the whole simulated domain, the mesh grid and the thickness of the PML layer (see further simulation details and convergence tests in Section S2).

4 | Results and Discussion

4.1 | MIM and MIMI Planar Waveguides

To relate the complex structure of plasmonic modes in the picopatch structure to simpler plasmonic waveguiding modes, we first consider the plasmonic modes in laterally-infinite Metal-Insulator-Metal (MIM) and Metal-Insulator-Metal-Insulator (MIMI) planar waveguides, as described by classical electromagnetic calculations within local dielectric response theory. The justification of this simple classical treatment is discussed at the end of this subsection. Crucially, the bare NPoM nanocavity (without the picopatch) supports Fabry-Pérot-like transverse cavity plasmons (TCPs) along the 1.1 nm-thick gap that originate from the reflection at the gap edges of the surface plasmon propagating in it [40–45]. The properties of this propagating surface plasmon can be obtained by studying an infinite MIM configuration that matches the local geometry of the NPoM gap, where the 'insulator' in the 'Metal-Insulator-Metal' structure is the dielectric in the gap. In a similar manner, the picopatch forms locally a MIMI (gold/vacuum slot/gold monolayer/dielectric) multilayer structure that supports propagating plasmons, which are reflected at the picopatch edges and lead to an additional set of Fabry-Pérot-like TCP modes. We do not include an additional metallic layer in the MIMI waveguide, corresponding to the nanoparticle at the top, because its effect on the dispersion is relatively weak. Understanding the dispersion of the MIM and MIMI modes is

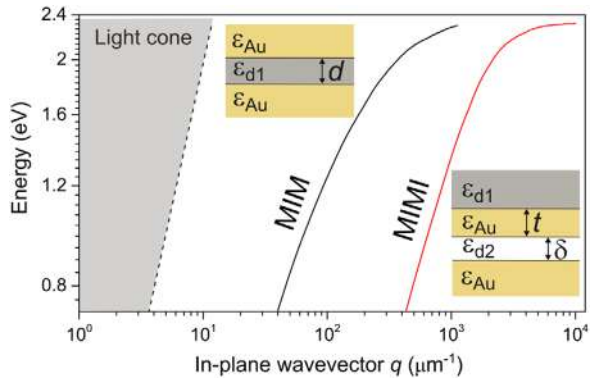

FIGURE 2 | Laterally infinite MIM and MIMI waveguides. Dispersion relationships of propagating plasmon modes in the planar MIM (black line) and MIMI (red line) configurations shown in the insets. The light cone of free photons in vacuum is represented by the gray area. Notice the logarithmic scale used here. The MIM structure consists of two semi-infinitely-thick Au films separated by a dielectric layer of permittivity $\varepsilon_{d1} = 2.1$ and thickness $d = 1.1$ nm (top inset). The MIMI structure consists of a semi-infinitely-thick Au film, a vacuum layer of permittivity $\varepsilon_{d2} = 1.0$ and thickness $\delta = 0.2$ nm, a thin gold layer of thickness $t = 0.235$ nm, and a semi-infinitely-thick dielectric layer of permittivity $\varepsilon_{d1} = 2.1$ (bottom-right inset). The MIM and MIMI dispersions are plotted as a function of the in-plane wavevector q. The dispersion of the MIM and MIMI modes tends toward zero energy for vanishingly small wavevectors (not evident in the figure because of the logarithmic scale).

crucial to later analyze the optical response of the full system (that is, the NPoM containing a picopatch).

The infinite MIM waveguide corresponding to the local configuration of the nanogap in the NPoM nanocavity is depicted in the top inset of Figure 2. This configuration is composed of a gold semi-infinite layer (permittivity ε_{Au}), a dielectric layer (permittivity $\varepsilon_{d1} = 2.1$) of typical thickness $d = 1.1$ nm, and a second gold semi-infinite layer. Using classical electromagnetic theory, the dispersion of these MIM waveguide modes [46] can be obtained by solving the following Equation (1),

$$\tanh\left(\frac{id}{2}\sqrt{k_0^{\,2}\varepsilon_{d1}-q^2}\right)=\frac{\varepsilon_{d1}}{\varepsilon_{Au}}\sqrt{\frac{q^2-\varepsilon_{Au}k_0^{\,2}}{q^2-\varepsilon_{d1}k_0^{\,2}}} \tag{1}$$

where k_0 is the vacuum wavevector, and q is the in-plane plasmonic wavevector of the propagating MIM plasmonic mode, i.e., the component parallel to the layers (x-axis) of the wavevector of the plasmonic excitation (see Section S1.1 for the derivation of Equation (1)).

On the other hand, the MIMI multilayer, corresponding to the local structure in the picopatch (bottom-right inset in Figure 2), consists of a thin gold layer of thickness $t = 0.235$ nm separated by a $\delta = 0.2$ nm thick vacuum layer (permittivity $\varepsilon_{d2} = 1.0$) from a semi-infinite Au surface (permittivity ε_{Au}) underneath. On top of the thin Au layer there is a semi-infinite dielectric layer (permittivity $\varepsilon_{d1} = 2.1$). The classical non-retarded dispersion of the MIMI plasmons confined in the subatomic-thick slot layer can be obtained by considering that the in-plane wavevector q is very large [33] (see Section S1.2). We obtain that the plasmonic MIMI modes verify,

$$\left(\frac{\varepsilon_{Au}-\varepsilon_{d1}}{\varepsilon_{Au}+\varepsilon_{d1}}\right)\left(\frac{\varepsilon_{Au}-\varepsilon_{d2}}{\varepsilon_{Au}+\varepsilon_{d2}}\right)\left[\left(\frac{\varepsilon_{Au}+\varepsilon_{d1}}{\varepsilon_{Au}-\varepsilon_{d1}}\right)\left(\frac{\varepsilon_{Au}-\varepsilon_{d2}}{\varepsilon_{Au}+\varepsilon_{d2}}\right)-\left(\frac{(\varepsilon_{Au}+\varepsilon_{d1})(\varepsilon_{Au}-\varepsilon_{d2})}{(\varepsilon_{Au}-\varepsilon_{d1})(\varepsilon_{Au}+\varepsilon_{d2})}-e^{-2qt}\right)\left(1-e^{-2q\delta}\right)\right]-1=0, \tag{2}$$

with q the in-plane plasmonic wavevector of the propagating MIMI plasmonic mode.

The dispersion curves of the MIM and MIMI (i.e., the energy of the corresponding propagating surface plasmons as a function of the in-plane wavevector q) are obtained from Equations (1) and (2) and are plotted in Figure 2 as black and red lines, respectively. For reference, the light cone of the free space photons ($\omega \geq ck_0$ with k_0 wavevector in vacuum) is represented by the gray area. The in-plane wavevector of surface plasmons propagating in the 1.1 nm-thick MIM waveguide is one order of magnitude larger than the vacuum wavevector for the energies considered [47], $q \approx 10k_0$. Remarkably, the MIMI mode in-plane wavevector is an additional order of magnitude larger than that of the MIM, and thus presents a hundred-fold wavevector mismatch when compared to that of the free photons, $q \approx 100k_0$. Such a huge q is behind the capability of picopatches to confine light into extremely small regions. However, the large mismatch in q between the MIMI mode and free photons also indicates that this plasmonic mode cannot be excited directly by incident light, making it challenging to optically exploit this mode in a planar system. A nanoresonator locally containing a MIMI can be used to overcome this limitation, as shown in the next section where we analyze the optical response of a localized MIMI structure (the picopatch) located within a large NPoM resonator. We note further that the MIMI plasmon dispersion exhibits a nearly linear dependence on the in-plane wavevector q up to energy ~ 2.2 eV (red line), indicating that this mode can be categorized as an acoustic excitation [48–50].

This analysis has considered a local classical permittivity of gold. The validity of this treatment for the very small thickness and separation distances involved in the MIMI structure was examined using full quantum ab-initio calculations in our recent work [33]. The dispersion obtained from the quantum theory was found to match the classical dispersion surprisingly well for thicknesses larger than a very small threshold separation distance, $\delta \gtrsim 0.2$–0.3 nm, and the field spatial distribution also showed good agreement for the thicknesses larger than this value. These results provided compelling evidence that the adopted classical electromagnetic theory is capable of reproducing well many of the features of the ab-initio calculations, even for an extremely thin gap as far as it is larger than the $\delta \approx 0.2$–0.3 nm threshold. This justifies the use of full-wave classical electromagnetic simulations in the following. On the other hand, the spectral width of the peak in the ab-initio calculations was broader (sometimes narrower) than that of the classical results, depending on the in-plane wavevector q, which indicates changes in the absorption losses that will affect the field enhancement in the nanoresonators. Notably, the local classical description does not include electron tunneling and non-local quantum effects

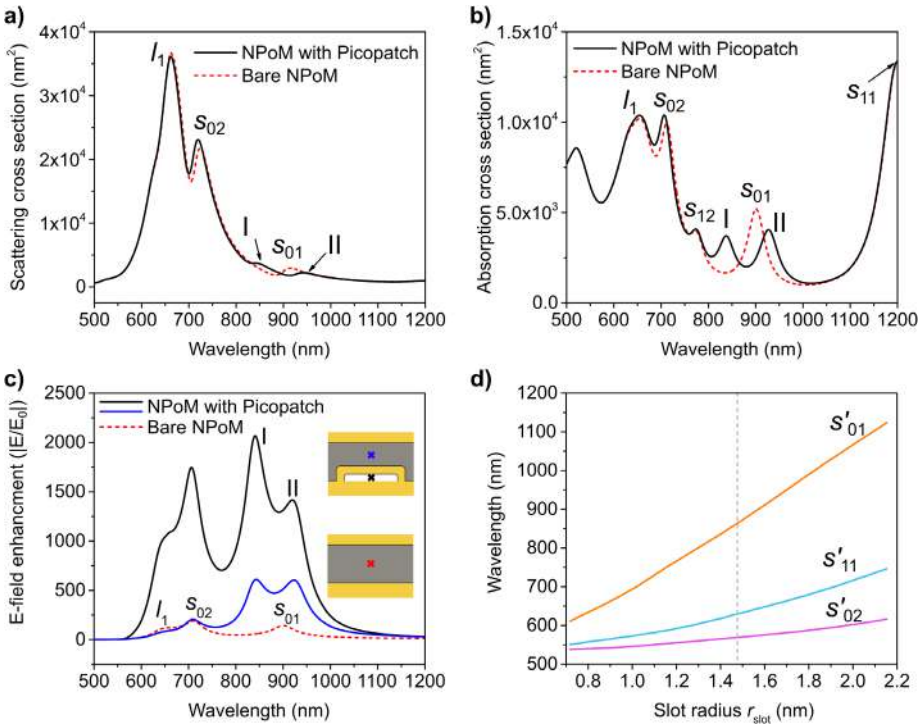

FIGURE 3 | Optical response of bare NPoM and NPoM containing a picopatch. (a) Scattering and (b) absorption cross section spectra (in nm^2), and (c) E-field enhancement spectra ($|E/E_0|$) in the absence (bare NPoM; red dashed line) and presence (NPoM with picopatch; black and blue solid lines) of the picopatch. The field enhancement is obtained at the center of the gap of the bare NPoM nanocavity without picopatch (red dashed line; position marked by red cross in the bottom inset) or, when the picopatch is included, at the center of the slot formed between the metal substrate and the thin metal layer of the picopatch (solid black line; black cross in the top inset and in Figure 1c) and near the center of the nanogap (blue line, blue cross in the top inset; see e.g. Figure S11 for discussion of the exact position of the evaluated fields). Results in (a-c) are obtained for the following parameters: $r_{sphere} = 40$ nm, $r_{facet} = 30$ nm, $d = 1.1$ nm, $\delta = 0.2$ nm, $t = 0.235$ nm, and $r_{slot} = 1.435$ nm. (d) Resonant wavelength of the modes of the picopatch (s'_{mn}, picopatch modes) as a function of the slot radius r_{slot} in the picopatch. The wavelength is obtained from analytical Equations (2) and (4), which do not include coupling with other modes. The values of the parameters other than r_{slot} are the same as in (a-c). Vertical dashed line corresponds to the value of $r_{slot} = 1.435$ nm used in (a-c).

such as Landau damping and electron spill-out that can increase losses [51–54], and thus be responsible for the modifications in plasmon widths. The effect of the possible underestimation of the absorption losses in the classical calculations is considered at the end of this work.

4.2 | Plasmonic Properties of Bare NPoM and NPoM with Picopatch

To better identify the effect of the picopatch, we first consider the optical response of bare NPoM resonators, corresponding to the structure in Figure 1c after removing the picopatch. As previously introduced, the system is illuminated by a p-polarized plane wave incoming at a 45^0 angle. The simulated spectra of the scattering cross section, the absorption cross section and the near-field enhancement $|E/E_0|$ at the nanogap center are shown by the red dashed lines in Figure 3a–c ($|E|$ amplitude of the induced electric field; $|E_0|$ corresponding value for the incident plane wave that excites the system). Following the nomenclature adopted previously [19, 20], we attribute the peak at the wavelength $\lambda \approx 660$ nm to the fundamental longitudinal antenna plasmon (LAP) mode (l_1) and the remaining peaks to transverse cavity plasmons (TCPs) of different orders (s_{mn}). The former (l_1) is characterized by the excitation of currents normal to the substrate (z direction). The latter (s_{mn}) are Fabry-Pérot-like modes induced by the reflection at the gap edges of the plasmons confined to the gap and propagating parallel to the gap interfaces (x-y plane), with the wavevector given by the MIM dispersion (black line in Figure 2). The s_{mn} mode is characterized by a spatial electric field distribution in the gap that approximately follows $E_z(\rho, \varphi) \approx J_m(a'_{mn}\,\rho/r_{facet})\cos(m\varphi)$, with E_z the z component of the field, J_m the Bessel function of the first kind, a'_{mn} the n^{th} root of the derivative of this function, and ρ and φ the radial and azimuthal coordinates [45, 55] (a related but different nomenclature is used in, e.g., Refs. [20, 56]). Thus, the subindexes (m, n) in s_{mn} refer to the symmetry of the different orders of the modes, with m the number of nodes in the azimuthal direction (φ in the range $[0, \pi]$) and n the number of nodes in the radial direction (ρ in the range $[0, r_{facet}]$). The assignment of these eigenmodes of the bare NPoM nanocavity is discussed in more detail below and in Section S3 (Figures S4 and S5).

The signature of the s_{mn} modes can be identified more clearly in the absorption cross section (Figure 3b, red dashed line), with the s_{02}, s_{12}, s_{01} and s_{11} modes appearing as peaks at increasing wavelengths. In contrast, the s_{11} and s_{12} modes are not distinguishable in the scattering spectra (Figure 3a, red dashed line) because these modes radiate weakly ('dark modes'), nor in the near-field enhancement evaluated in the gap center (Figure 3c, red dashed

line) because these modes present a zero value at this position due to their symmetry. Additionally, the s_{01} mode appears in the scattering as a Fano-like resonance due to the interference with the background response coming from higher-energy modes [57–59]. A similar interference effect could also explain why the s_{02} peak appears at a slightly different wavelength in the scattering ($\lambda \approx 725$ nm) and in the absorption ($\lambda \approx 710$ nm) spectra. We further highlight that the maximum electric field enhancement for bare NPoM that appears at the peak associated with the s_{02} mode is $|E/E_0| \approx 200$.

We consider next the response of the NPoM containing a picopatch (sketched in Figure 1c) under the same plane wave illumination. The spectra of the scattering and absorption cross sections, as well as the field enhancement spectra evaluated in the center of the picopatch slot (position marked by a black cross in the top inset in Figure 3c as well as in Figure 1c), are shown by black solid lines in Figure 3a–c. The scattering (Figure 3a) and absorption (Figure 3b) cross section spectra of the NPoM containing a picopatch are generally very similar to those of the bare NPoM (compare black lines and red-dashed lines). However, in the spectral region near $\lambda = 900$ nm, the s_{01} peak in the bare NPoM spectra splits into two (marked as "I" and "II") when the picopatch is included. This splitting is due to the strong coupling between the s_{01} nanocavity mode and a new Fabry-Pérot-like TCP mode associated with the picopatch (s'_{mn} picopatch modes in the following), resulting in these two hybrid modes. It is remarkable that this substantial change, which may be accessible in far-field experiments and thus be used to detect the formation of picocavities [34], can be induced by such a small change in the local geometry (extending over a height $t + \delta = 0.435$ nm and a radius $r_{slot} + 0.235$ nm $= 1.67$ nm, and thus a volume of only ≈ 3.8 nm^3). Additionally, the presence of the picopatch results in a small shift of the s_{02} nanocavity mode.

The effect of the picopatch is much more dramatic when considering the local fields (Figure 3c). The s_{01} peak in the bare NPoM spectra evaluated in the center of the nanogap (red dashed line) near $\lambda = 900$ nm splits again into two in the spectra calculated in the center of the slot when the picopatch is present (black solid line). Importantly, the electric field enhancement inside the slot is greatly enhanced by the picopatch, approximately one order of magnitude, up to $|E/E_0| \approx 2000$. Furthermore, the blue line in Figure 3c shows that the picopatch also strongly enhances the field spectra, up to $|E/E_0| \approx 600$, at the region of the nanogap over the picopatch (position indicated by the blue cross in the top inset), which could be exploited in spectroscopy measurements of molecules placed in this region.

We analyze next in more detail the Fabry-Pérot-like s_{mn} and s'_{mn} transverse cavity plasmon (TCP) modes. As introduced above, both the NPoM nanogap and the subatomic-thick slot can behave as waveguides with finite boundaries, which thus discretize the continuum of propagating MIM or MIMI modes into localized plasmon states. These states emerge when the modes that propagate parallel to the nanocavity gap or the picopatch slot reflect at the gap or slot edges, respectively, and interfere constructively, analogously to the resonances of a Fabry-Perot resonator [19, 42, 60, 61]. The resulting Fabry-Perot-like resonances contribute to two sets of TCP modes, associated with either the nanocavity (s_{mn}) or the picopatch (s'_{mn}). Both sets of modes are present in the NPoM resonator containing the picopatch. Ignoring the interaction between different modes, the resonant plasmonic wavelength λ_{pl} of the set of nanocavity TCP modes (s_{mn}) can be obtained from Refs. [45] and [55], giving

$$\lambda_{pl} = \frac{2\pi r_{facet}}{a'_{mn}} \tag{3}$$

where r_{facet} is the radius of the bottom flat facet of the gold nanosphere, and a'_{mn} is the nth root of the derivative of the Bessel function of order m, J_m. On the other hand, we approximate the resonant plasmonic wavelength λ'_{pl} of the set of the picopatch TCP modes (s'_{mn}) as

$$\lambda'_{pl} = \frac{2\pi r_{slot}}{a_{mn} - \beta} \tag{4}$$

Here, r_{slot} is the radius of the subatomic-thick slot, and we consider the nth root of the Bessel function of order m (a_{mn}), instead of its derivative, and include a reflection phase [62, 63] $\beta = \pi/4$. The difference between Equations (3) and (4) can be understood from the contrast between the spatial field distribution of the two types of modes. The fields of the s_{mn} modes present approximately a local maximum at the nanocavity edge, while the field of the s'_{mn} modes is closer to a minimum at the edge of the slot (see Figure 5b,d below). We attribute this difference to the contrast in the terminations of the cavity: the picopatch slot is 'close', i.e., with metals at the edges, contrary to the 'open' nanogap limited laterally by vacuum. We do not attempt to assess the validity of Equation (4) for general systems, but we have found it suitable to model the response of the structure considered in this work. The resonant vacuum wavelength of the different modes can then be obtained theoretically using the dispersion of the waveguide modes (Equation (1) or Equation (2)) together with the resonant conditions (Equation (3) or Equation (4)).

Figure 3d shows the expected dependence of the resonant vacuum wavelength of the picopatch TCP modes on slot radius r_{slot} for different orders (m, n), as given by the analytical Equations (2) and (4) (the nanocavity modes are discussed in Section S3). The picopatch modes (s'_{mn}) redshift clearly with increasing r_{slot}, especially for the lowest-order s'_{01} mode. When r_{slot} is increased from ~ 0.7 nm to ~ 2.1 nm (a very small change in geometry), the s'_{01} mode can be tuned from a vacuum wavelength of $\lambda \approx 610$ nm to $\lambda \approx 1100$ nm, covering wavelengths from the visible to well into the near-IR region. The predicted presence of plasmonic modes for such extremely small lateral size of the picopatch ($r_{slot} \approx 1$–2 nm) is remarkable, and is only possible because of the very small thickness of the picopatch.

For the slot radius $r_{slot} = 1.435$ nm used in Figure 3a–c, the predicted s'_{01} mode is found near $\lambda = 850$ nm in Figure 3d (as marked by the vertical dashed line). This wavelength is close to the s_{01} mode of the NPoM nanocavity. Thus, the peaks observed in the spectra of Figure 3b,c at $\lambda \approx 830$–930 nm (black solid lines) can be attributed to the coupling between the s'_{01} and s_{01} modes, which results in two new hybridized modes. Next, we discuss further this hybridization and the validity of the analytical model that leads to Equations (2) and (4).

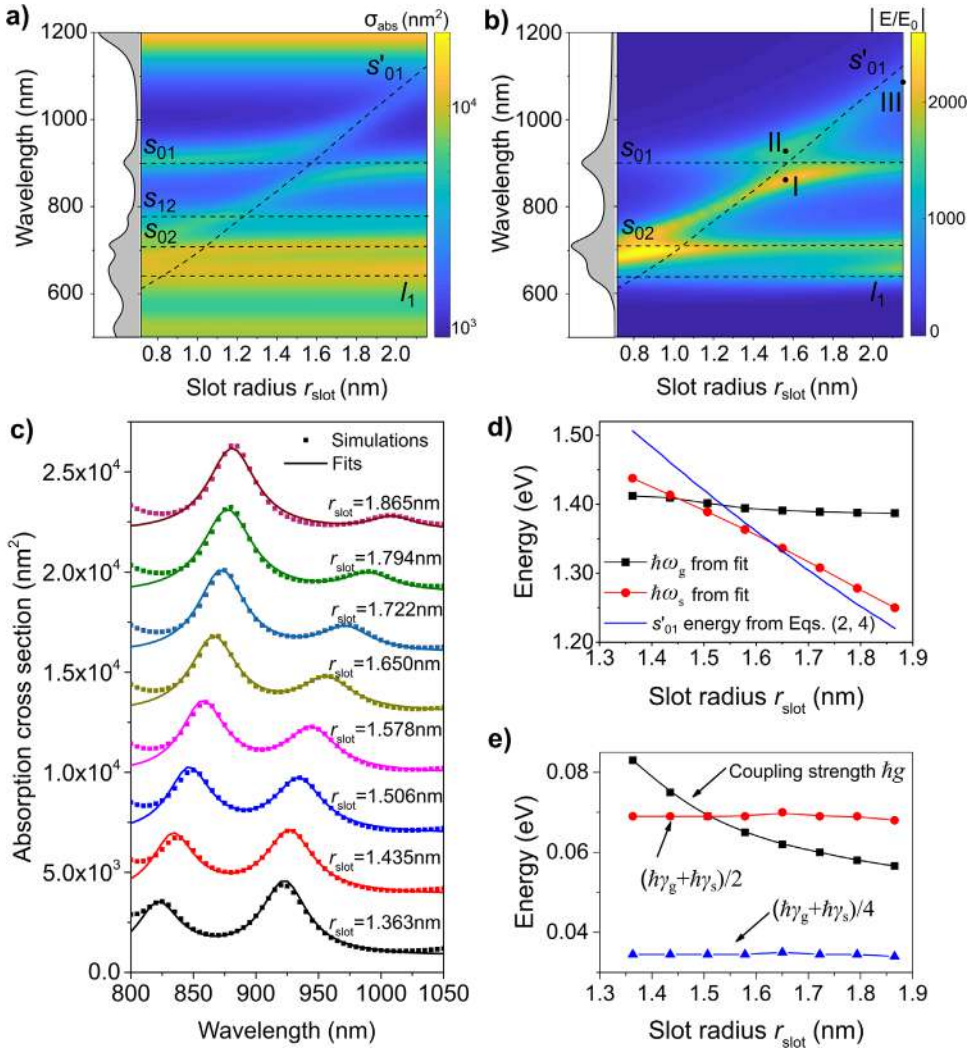

FIGURE 4 | Mode hybridization and fitting based on the two coupled-oscillator model. (a, b) Color maps of (a) the absorption cross section (in nm^2), and (b) the electric field enhancement $|E/E_0|$ (evaluated in the center of the slot formed between the metal substrate and the thin metal layer of the picopatch, marked by a black cross in Figure 1c). These color maps are calculated as a function of the wavelength λ and the slot radius r_{slot} (sketch in Figure 1c). The spectra to the left of each color map are the corresponding results for the bare NPoM nanocavity, consisting of the same system after removing the picopatch. The horizontal dashed lines indicate the position of the bare NPoM nanocavity eigenmodes. The theoretical wavelength of the s'_{01} mode introduced by the picopatch is shown by the diagonal dashed line, as obtained from Equations (2) and (4) that do not include coupling between modes. Labels 'I', 'II', and 'III' correspond to conditions to be examined more in detail in Figure 5. (c) Fittings of the absorption spectra obtained for r_{slot} = 1.363 -1.865 nm and wavelength between λ = 800 and 1050 nm. The fitting uses Equation (5), derived from a coupled harmonic oscillator model, as discussed in the text. The dots correspond to the simulations, and the solid lines to the fits. Note that absorption spectra are shifted vertically for clearer visualization. (d) Resonant energies of the s_{01} ($\hbar\omega_g$, black square dots) and s'_{01} ($\hbar\omega_s$, red circle dots) modes extracted from the fits for different values of r_{slot}, together with the resonant energy of the s'_{01} mode predicted by Equations (2) and (4) (blue solid line; these results are the same as those given by the diagonal dashed line in (a) and (b)). (e) Coupling strength $\hbar g$ between the s'_{01} and s_{01} modes (black square dots) and damping rates of the s'_{01} and s_{01} modes (red circle dots: $\hbar(\gamma_g+\gamma_s)/2$; blue triangles: $\hbar(\gamma_g+\gamma_s)/4$), extracted from the fits for different values of r_{slot}.

4.3 | Hybridization of Nanocavity and Picopatch Modes

We can exploit the tunability of the s'_{01} picopatch TCP mode with changes of the picopatch size (specifically the slot radius r_{slot}). This approach serves to analyze in more detail the hybridization of this mode with other modes of the NPoM resonator. The 2D color maps in Figure 4a,b show the dependence of the simulated absorption cross section and near-field enhancement ($|E/E_0|$) on the excitation wavelength λ and slot radius r_{slot} (the corresponding dependence of the scattering cross section spectra is given in Figure S6). The spectra to the left of the color maps correspond to the reference results for the same system but without the picopatch (bare NPoM nanocavity). Horizontal dashed lines are also included in the 2D color maps to mark the position of the bare NPoM nanocavity modes (l_1 and s_{mn}), as extracted from the simulations in the absence of picopatch. Last, the theoretical wavelength of the picopatch mode (s'_{01}) as a function of r_{slot}, according to Equations (2) and (4), is indicated by the diagonal dashed line.

For most values of r_{slot}, the NPoM nanocavity s_{mn} modes are unaffected or weakly affected by the presence of the picopatch, as indicated by the presence of broad horizontal bands in the color maps. The observed modification and shift of these modes is a remarkable effect considering the tiny size of the picopatch, but the change is often small. An exception occurs for illumination wavelengths at $\lambda \approx 800$–1000 nm and slot radius $r_{slot} \approx 1.4$–1.8 nm. In this region, the spectral peaks show a clear anti-crossing behavior that can be understood as being due to the coupling between the s_{01} nanocavity mode (horizontal dashed line) and the s'_{01} picopatch mode (diagonal dashed line). We emphasize that the horizontal and diagonal dashed lines mark the evolution of these modes in the absence of coupling, obtained respectively from the simulation of the bare NPoM nanocavity without picopatch and from the theoretical model.

The anti-crossing is observed when the s'_{01} mode is tuned to the wavelength of the s_{01} mode, and is a consequence of the strong coupling between them [64–69], giving rise to the two new hybrid modes labeled 'I' and 'II', as indicated in Figure 3a–c. Additionally, this hybridization leads to a particularly efficient coupling of the incoming light into the subatomic-thick vacuum slot in the picopatch, as the top Au nanoparticle acts as a nanoantenna that feeds light into the NPoM nanogap mode coupled to the picopatch. This behavior results in the strongly enhanced E-fields shown in Figure 4b. Very strong electric-field enhancements are also found when the s'_{01} mode is tuned close to the wavelength of the s_{02} nanocavity mode, but in this case the presence of an anti-crossing behavior is less clear. In addition, the absorption map in Figure 4a exhibits a crossing behavior between the s'_{01} picopatch mode and the s_{12} nanocavity mode around the wavelength of $\lambda \approx 775$ nm and slot radius of $r_{slot} \approx 1.2$ nm. This behavior is a signature of the absence of (or weak) coupling between these modes, a consequence of the different symmetry of their associated near fields (compare the near fields in Figures S5b and S7a).

To confirm the strong coupling between the s'_{01} and s_{01} modes, we fit the simulated absorption cross section spectrum of the NPoM with picopatch in the anti-crossing spectral region (near $r_{slot} \approx 1.5$ nm and $\lambda \approx 875$ nm) to the analytical expression derived from a coupled harmonic oscillator model [70, 71],

$$\sigma_{ext}(\omega) \propto \omega\, Im\left\{ \frac{\omega_s^2 - \omega^2 - i\omega\gamma_s}{\left(\omega_g^2 - \omega^2 - i\omega\gamma_g\right)\left(\omega_s^2 - \omega^2 - i\omega\gamma_s\right) - 4g^2\omega^2} \right\} \quad (5)$$

where Im{} refers to the imaginary part, ω_g and ω_s are the resonant frequencies of the s_{01} and s'_{01} modes, γ_g and γ_s are their corresponding damping rates, and g is the coupling strength between them. These resonant frequencies and damping rates are those of the bare modes, i.e., the modes that would be present if the coupling could be switched off. All parameters in Equation (5) (except ω) are fitting parameters that vary with r_{slot}. In the fitting procedure, we also include a r_{slot}-dependent constant background and make sure that ω_g (corresponding to the s_{01} mode in the nanogap) and γ_g (corresponding to the damping rate of the s_{01} mode) only experience small variations around the value obtained for the bare NPoM nanocavity ($\hbar\omega_g = 1.4$ eV and $\hbar\gamma_g = 0.07$ eV). Notice that two slightly different versions of the coupled oscillator model have been used in the literature [72], but the results obtained for our system should not depend significantly on this choice. Additionally, Equation (5) corresponds to the expression of the extinction spectra instead of the absorption, but this choice is not expected to result in any substantial difference in the values of coupling and anti-crossings extracted.

Figure 4c shows the fittings for $r_{slot} = 1.363$–1.865 nm and wavelength between $\lambda = 800$ and 1050 nm, with the simulated absorption spectra shown by the dots, and the result of the fit shown by solid lines. The fit is very satisfactory. The coupling strength g, resonant frequencies (ω_g and ω_s), and both a half $(\gamma_g+\gamma_s)/2$ and a quarter $(\gamma_g+\gamma_s)/4$ of the total damping rates, extracted from all fittings, are plotted in Figure 4d,e. The black square dots in Figure 4d show that the extracted resonant energy $\hbar\omega_g$ is always similar to the resonant position of the s_{01} nanocavity mode ($\hbar\omega_g = 1.4$ eV, $\hbar$ reduced Planck's constant). In contrast, the extracted resonant energy $\hbar\omega_s$ (red circle dots in Figure 4d) presents a nearly linear shift with the change of r_{slot}, in good overall agreement with the s'_{01} picopatch mode energies obtained with the analytical model (Equations (2) and (4)), which are also shown in Figure 4d (blue solid line). This agreement further supports the validity of the analytical model to describe the (uncoupled) picopatch modes.

To determine whether we are in the weak or strong coupling regime, we compare in Figure 4e the value of the extracted coupling strength g with the damping rates of the two resonant modes. The coupling strength g decreases moderately with increasing slot radius r_{slot} (black square dots in Figure 4e), but, more importantly, it is always very large, $\hbar g \approx 50$–80 meV. Thus, the frequently-used criteria to identify the strong coupling regime, $g \geq (\gamma_g+\gamma_s)/4$, is always amply satisfied ($(\gamma_g+\gamma_s)/4$ is shown by the blue triangles in Figure 4e). Further, even the more demanding criteria, $g \geq (\gamma_g+\gamma_s)/2$, is satisfied for $r_{slot} \lesssim 1.5$ nm ($(\gamma_g+\gamma_s)/2$ is shown by red circle dots in Figure 4e). These results confirm that the extremely confined picopatch mode and the nanocavity mode are strongly coupled [65, 73].

4.4 | Near-Field Distribution and Effective Mode Volume

To complete our analysis of the picopatch and NPoM nanocavity modes and their coupling, we show in Figure 5 the spatial distribution of the normalized amplitude of the electric field ($|E/E_0|$), i.e. field enhancement maps, of several relevant modes (plotted in the vertical x-z and horizontal x-y planes). Figure 5a,b correspond to the uncoupled mode of the bare NPoM nanocavity at $\lambda = 895$ nm (see red dashed lines in Figure 3a–c). The fields and associated surface charges induced at the interfaces (the latter denoted schematically by '+' and '-') show an almost rotationally-symmetric standing-wave pattern with local maximum near the nanogap edge and strongest fields in the central region of the nanogap, which confirms the assignment of this peak as the s_{01} TCP mode of the nanocavity.

To analyze the uncoupled s'_{01} picopatch mode, we plot in Figure 5c,d the field enhancement $|E/E_0|$ and corresponding charge distributions near the picopatch, for slot radius $r_{slot} = 2.153$ nm and wavelength $\lambda = 1080$ nm (conditions marked with

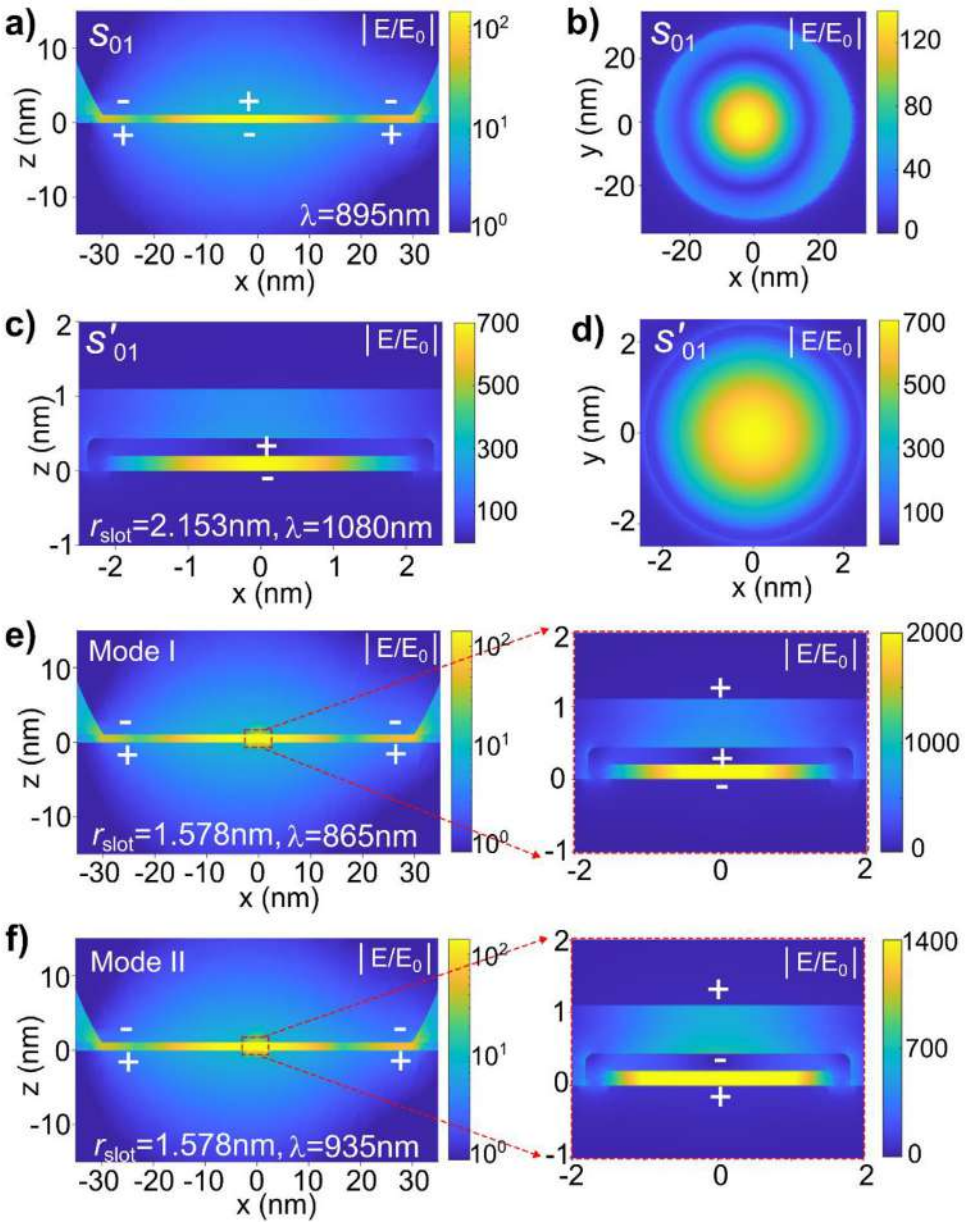

FIGURE 5 | Near-field spatial distributions of different nanocavity and picopatch modes. (a, b) Field enhancement ($|E/E_0|$) maps of uncoupled nanocavity mode s_{01} (obtained at $\lambda = 895$ nm for the bare NPoM without picopatch). (c, d) Field enhancement ($|E/E_0|$) maps of the (almost) uncoupled picopatch mode s'_{01} (obtained at $\lambda = 1080$ nm for the NPoM containing a picopatch with $r_{slot} = 2.153$ nm; condition marked by dot with label "III" in Figure 4b). (e, f) Field enhancement ($|E/E_0|$) maps of the hybrid modes marked "I" and "II" in Figure 4b (obtained at $\lambda = 865$ nm and $\lambda = 935$ nm, respectively, for the NPoM containing a picopatch with $r_{slot} = 1.578$ nm). (a, c, e, f) show the fields in the vertical x-z plane that contains the center of the nanogap (y = 0) (side view). (b, d) show the fields in the horizontal x-y plane (top view), corresponding to (b) z = 0.55 nm (crossing the nanogap center) and (d) z = 0.1 nm (crossing the slot center). The left panels in (e, f) show the fields in the nanogap, and those on the right a zoom into the region of the picopatch. Notice that the region plotted in (c, d) is significantly smaller than in (a, b) (see the x and y labels). The colormap is logarithmic in (a) and left panels of (e, f) and linear in other plots (including right panels of (e, f)). The x and z directions are indicated in the axis and in Figure 1c, with the center of the nanogap corresponding to x = y = 0, z = 0.55 nm.

'III' in Figure 4b). These conditions are chosen to minimize the interaction of the s'_{01} with the s_{01} nanocavity mode, due to a large detuning between the frequency of these two modes. The fields, which are again rotationally symmetric, show extremely large E-field enhancement ($|E/E_0| \approx 700$) confined to the tiny vacuum slot in the middle of the picopatch. The field distribution of the s'_{01} picopatch mode (Figure 5c,d), with maxima at the slot center and weaker fields at the slot edges, differs from that of the s_{01} nanocavity mode (Figure 5a,b) due to the different boundary conditions at the edges of the waveguides (closed and open, respectively, see discussion of Equations (3) and (4)). Higher-order picopatch modes (s'_{11} and s'_{02}) are discussed in Section S5 (see Figure S7).

The fields of the new hybrid modes emerging from the interaction of the s_{01} NPoM nanocavity and s'_{01} picopatch modes are calculated in the region of the anti-crossing (r_{slot} = 1.578 nm, and λ = 865 nm or λ = 935 nm, marked with 'I' and 'II' in Figure 4b) and plotted in Figure 5e (λ = 865 nm) and Figure 5f (λ = 935 nm). The associated charges induced at the metal-dielectric interfaces are again indicated schematically. The hybrid-mode fields combine features from the two original uncoupled modes, with the strongest fields located in the picopatch slot (see zooms in the right panels in (e, f)) but also strong fields at the center and near the edges of the nanocavity. Consistent with hybridization theory [74, 75], these electric field distributions can be understood as the sum of the contributions from the s_{01} and s'_{01} modes, with a phase difference between these contributions that depends on the specific hybrid mode: relative phase 0 for hybrid mode 'I' and π (sign change) for hybrid mode 'II', corresponding to symmetric and anti-symmetric combinations of the uncoupled plasmon modes. The relative phase can be appreciated in the figures by comparing the sign of the charges at the edges of the nanogap (set by the s_{01} mode contribution) with those at the picopatch (dominated by the s'_{01} mode contribution). The sign at the gap edges is the same in Figure 5a,e,f, but the sign at the picopatch is opposite in the hybrid mode 'II' (Figure 5f) compared to the hybrid mode 'I' (Figure 5e) and the uncoupled picopatch mode (Figure 5c). For completeness, note that the sign of the charges at the center of the top surface of the nanocavity – 0.665 nm over the picopatch—seems to be set mainly by the uncoupled s_{01} nanocavity mode, explaining why they have the same sign for both hybrid modes.

Additionally, the field distribution highlights that the fields in the vacuum slot of the picopatch are substantially enhanced when the hybrid modes are excited, with the enhancement factors reaching up to $|E/E_0| \approx 2000$. The fields can also significantly penetrate inside the metal, reaching $|E/E_0| \approx 300$ at the picopatch thin metallic layer (Au monolayer), which is consistent with recent work suggesting that the field increase associated with the random formation of picopatches could explain short-lived experimental increases (flares) of the inelastic light emission from gold nanogaps [34, 35]. From the opposite perspective, it may be possible to use the flares to assess the experimental field enhancement in the picopatch. Last, the electric fields at the top of the picopatch, i.e., the region between the nanocavity upper interface and the gold monolayer below, are significantly smaller than in the slot but still very large (up to $|E/E_0| \approx 600$, compared to $|E/E_0| \approx 200$ in the case of the bare NPoM resonator; see also Figure 3c). Since this region is available for molecules or emitters, the large field enhancement could therefore be useful in molecular spectroscopy, and the enhancement of the spectroscopic signal may also introduce a path to calibrate the field enhancement [76, 77].

The extremely large field enhancement and field concentration at the picopatch slot suggest that the effective mode volume (V_{eff}) of the hybrid modes is very small. Here, V_{eff} refers to the volume that determines the local density of states (LDOS $\propto 1/V_{eff}$) of a given mode and thus how much the mode can enhance different light-matter interactions in a quantum mechanical description, and not just to the volume of a 'hot spot' region of strong fields.

To reach very small V_{eff} is significantly more challenging than obtaining 'hot spots' of the same volume. V_{eff} appears in the often-used expression of the Purcell Factor [78] and has been typically calculated using the electromagnetic energy [79, 80]. However, this approach can be inappropriate when losses are large, as in plasmonic systems [81–84], and an alternative approach based on quasi-normal modes has been developed to treat non-Hermitian (lossy) systems [85–88]. In this case, the effective volume $\tilde{V}$ is a complex-valued volume and can be obtained from the following Equation (6),

$$\tilde{V} = \frac{\int \left[\left(\frac{\partial(\omega\tilde{\varepsilon})}{\partial\omega} \right) \tilde{\mathbf{E}}_s^2 - \mu_0 \tilde{\mathbf{H}}_s^2 \right] d^3\boldsymbol{r}}{2\varepsilon_0 (\tilde{\mathbf{E}}(r_m) \cdot \boldsymbol{u})^2} \tag{6}$$

with $\tilde{\varepsilon}$ the position-dependent complex permittivity, ε_0 the vacuum permittivity, μ_0 the vacuum permeability, ω the (angular) frequency and $\tilde{\boldsymbol{E}}_s$ ($\tilde{\boldsymbol{H}}_s$) the position-dependent complex scattered electric (magnetic) field vector of the resonant mode under analysis. Note that Equation (6) takes into account that the slot is filled by vacuum, and that the integral extends over the whole computational domain. The complex Au permittivity (and its derivative) and the fields are evaluated at the corresponding resonant frequency. $\tilde{\mathbf{E}}(r_m) \cdot \boldsymbol{u}$ is the value of $\tilde{\boldsymbol{E}}_s$ at a given position projected to a unit vector $\boldsymbol{u}$, so that in the quasi-normal modes formalism $\tilde{V}$ is defined for a given location and orientation. Here, we choose the position to be the center of the slot inside the picopatch and $\boldsymbol{u}$ = (0, 0, 1) (z-axis), which corresponds (up to an excellent approximation) to the position of strongest field and to the orientation of this field. We make this choice because the resulting $V_{eff} = \mathrm{Re}\{\tilde{V}\}$ (Re{} indicating the real part) describes the field confinement in an analogous manner to the often-used convention in the analysis of normal modes where the mode volume is an intrinsic property that quantifies the confinement of a mode, without needing to specify any particular position [81, 89–91]. The imaginary part of the effective volume, $\mathrm{Im}\{\tilde{V}\}$, quantifies the losses of the system.

All the quantities involved in Equation (6), e.g. $\tilde{\mathbf{E}}_s$ and $\tilde{\mathbf{H}}_s$, are in principle evaluated at the complex-valued resonant frequency of the quasi-normal modes [86]. However, for simplicity, we fix the (real) frequency from the maxima in the absorption spectra, and obtain the scattered fields at this frequency under plane wave illumination. As the effective mode volume in Equation (6) is defined for a single mode, in these calculations we diminish *ad-hoc* the imaginary part of the Au permittivity by a factor of 10 (i.e., $\mathrm{Im}\{\varepsilon_{Au}\} \rightarrow \mathrm{Im}\{\varepsilon_{Au}\}/10$), which should not modify noticeably the value of $\mathrm{Re}\{\tilde{V}\}$ but suppresses the difficulties due to the off-resonant excitation of other modes.

Figure 6 shows the value of $V_{eff} = \mathrm{Re}\{\tilde{V}\}$, which describes the field confinement, as a function of r_{slot} for the two resonant hybrid modes (I and II) of the NPoM resonator with picopatch (black lines). At $r_{slot} \approx 1.650$ nm, the field confinement of both hybrid modes is similar and extremely small, $\sim 3.5\ \mathrm{nm}^3$. This value of r_{slot} is close to the value at which the frequencies of the uncoupled s_{01} and s'_{01} modes of the bare NPoM nanocavity and of the picopatch are the same in Figure 4d. As r_{slot} increases or decreases from 1.650 nm, the mode volume of one of the hybrid modes strongly increases, while the other decreases gradually. This

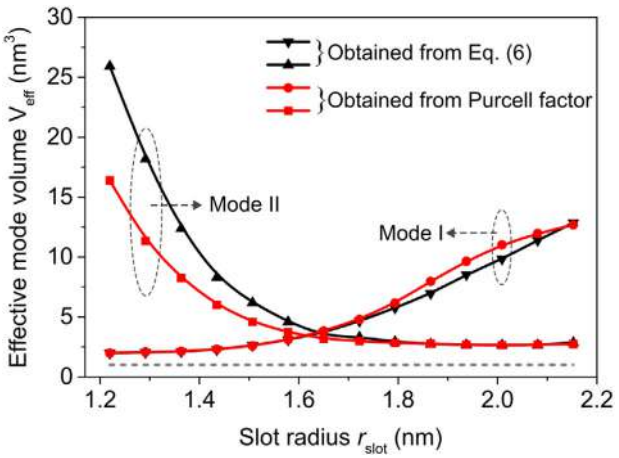

FIGURE 6 | Effective mode volume V_{eff} of the two hybrid modes of the NPoM with picopatch. V_{eff} is plotted as a function of the picopatch radius r_{slot}, obtained from the real part of Equation (6) (black lines) and from the Purcell factor (red lines). The reference value of mode volume of 1 nm^3 is indicated by the horizontal gray dashed line. The simulated system corresponds to the NPoM resonator with picopatch sketched in Figure 1c.

tendency follows the general expectation for the hybridization of the modes of very different effective mode volumes: as the detuning increases, the values of V_{eff} approach toward those of the uncoupled modes. In our case, the hybrid mode with smaller mode volume is mostly associated with the picopatch s'_{01} mode. For $r_{\text{slot}} \approx 1.2$ nm, the (real part of the) effective mode volume of this mode is only $V_{\text{eff}} \approx 1.8$ nm^3, similar to the geometrical volume of the slot ($V_{\text{slot}} \approx 0.9$ nm^3). We thus find that the effective mode volume of the NPoM resonator with picopatch can get close to 1 nm^3 (value marked for reference by the horizontal dashed line in Figure 6), and may become even smaller than this value for more optimized picopatch configurations, thus offering an excellent geometrical alternative to achieve extreme light confinement to the picocavities formed by isolated atomic-sized protrusions [23].

In order to further verify the value of V_{eff} obtained in Figure 6 with Equation (6) and real-valued frequencies, we also extract the effective mode volume from the Purcell factor [78] experienced by a dipole positioned at the center of the picopatch slot and perfectly aligned along the vertical z-axis. In Section S6, we describe this procedure in detail and plot the Purcell factor as a function of wavelength and slot radius (Figure S8). The effective mode volume for the two hybrid modes (I and II) of the NPoM resonator with picopatch, obtained from the Purcell factor, is plotted in Figure 6 (red lines). The values of the effective mode volume obtained in this way are in good overall agreement with the values of V_{eff} obtained from Equation (6). For reference, we also show in Figure S11 the Purcell factor at a different position in the gap. Last, as an additional verification of the validity of using real-valued frequencies to calculate $V_{\text{eff}} = \text{Re}\{\tilde{V}\}$ with Equation (6), we have also calculated this quantity for $r_{\text{slot}} = 1.435$ nm by evaluating Equation (6) with complex frequencies according to the full quasi-normal mode approach [85, 86, 88]. The values of V_{eff} obtained with the real and complex frequencies are almost identical, as discussed in more detail in Section S10.

4.5 | Robustness to Morphology and Losses

The picopatch that we have considered forms a vacuum slot of perfectly homogeneous thickness. However, the exact morphology of a picopatch cannot be controlled in current experiments where the picopatch would be formed through the random movement of gold atoms. To illustrate the influence of the shape of the picopatch on the plasmonic response of the system, we consider next the picopatch configuration sketched in Figure 7a. In this case, the top flat surface of the picopatch is replaced by a gold semi-ellipsoid of wall thickness $t = 0.235$ nm, so that a non-flat slot with a maximum height $\delta = 0.2$ nm and a radius at the bottom r_{slot} is formed below. Other than this modification, the rest of geometrical properties of the NPoM resonator with picopatch remain unchanged.

The absorption cross section spectra of the modified system with a non-flat picopatch and the corresponding electric field enhancement $|E/E_0|$ spectra (evaluated in the slot center) are shown by color maps in Figure 7b,c as a function of r_{slot}. A clear anti-crossing-like behavior is observed when the s_{01} mode associated with the bare NPoM nanocavity (marked by a horizontal dashed line) is resonant with the s'_{01} picopatch mode (the diagonal dashed line indicates the resonant wavelength of this mode in the absence of coupling with other modes, as given by Equations (2) and (4)). Crucially, the qualitative behavior remains the same as for the flat picopatch in Figure 4a,b, although a more careful comparison between Figure 4a,b and Figure 7b,c shows some differences. For example, the anti-crossing behavior is less clear for the semi-elliptical picopatch, with a smaller energy difference between the two hybrid modes, indicating a smaller coupling strength than the case in Figure 4a,b. Further, the maximum E-field enhancement reaches ~ 3000 for the semi-elliptical picopatch, even larger than for the flat picopatch. We thus find that the exact plasmonic response of the full system is sensitive to the geometrical details of the picopatch morphology, but the general behavior remains unchanged. For completeness, the scattering spectra of the modified system with a semi-elliptical picopatch is shown in Figure S9. We also note that changes of the picopatch morphology that break the rotational symmetry of the system would lift the degeneracy of some of the cavity modes and could lead to mode splitting also in the absence of strong coupling [92].

Last, we consider the effect of increased material losses on the response of the system. We discussed previously how quantum calculations confirm the existence of the slot mode in the MIMI configuration even for extremely thin layers, but the influence of quantum effects on the losses experienced by the slot mode is more challenging to assess. Nevertheless, in principle, we expect that the absorption in gold can be larger than that predicted from the classical permittivity due to non-local, and spill-out effects. To analyze to what extent the optical response of the system is sensitive to an increase in absorption losses, we artificially increase the imaginary part of the Au classical permittivity according to the expression,

$$\varepsilon_{Au} = \text{Re}\{\varepsilon_{Au}\} + if\ \text{Im}\{\varepsilon_{Au}\} \tag{7}$$

where the loss factor is $f = 1$ for the experimental values in Ref. [39] (i.e. the permittivity used in other simulations in this work when not stated otherwise) and $f > 1$ corresponds to increased

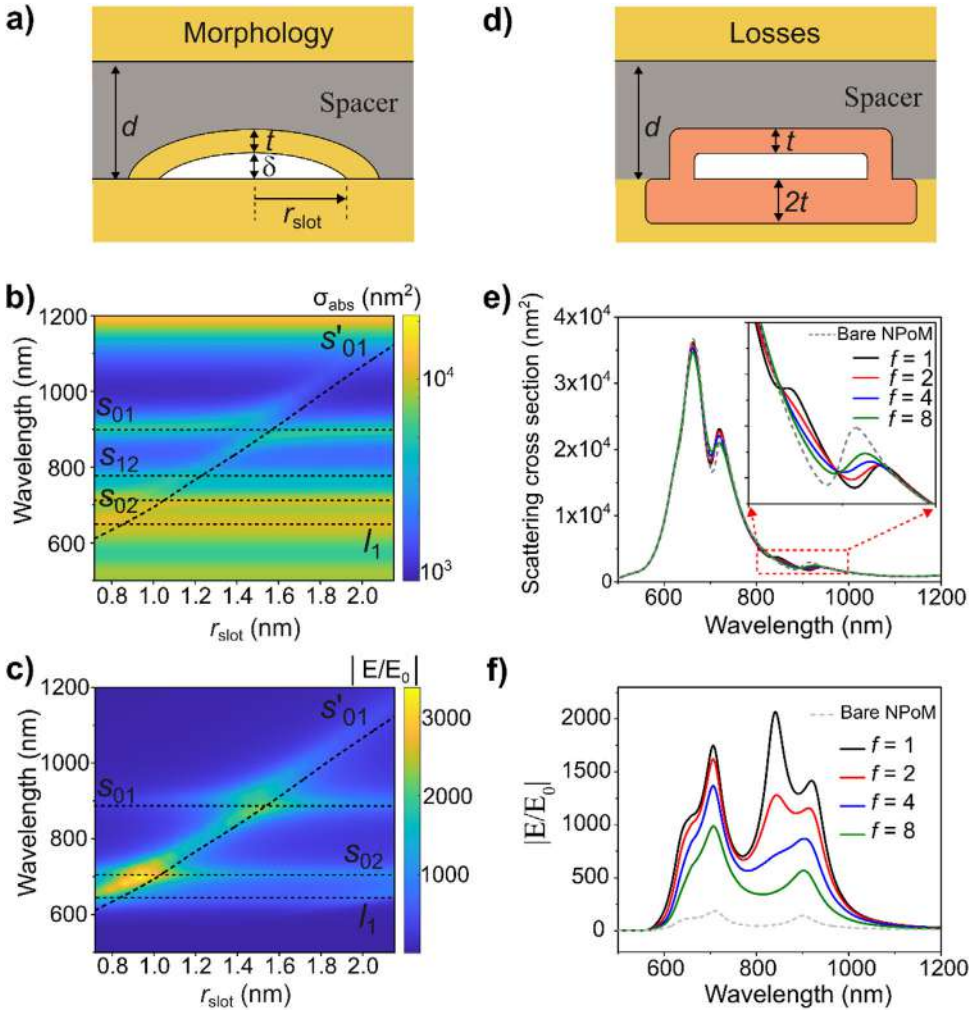

FIGURE 7 | Robustness of the response to the exact shape of the picopatch and to material losses. (a) Sketch (not to scale) of a modified picopatch morphology, where the top surface of the picopatch corresponds to a rotationally-symmetric semi-ellipsoid gold monolayer of thickness $t = 0.235$ nm, forming a vacuum slot with short semi-axis (height) of size $\delta = 0.2$ nm and long semi-axis (radius) of size r_{slot}. (b, c) Color maps of the (b) absorption cross section (in nm^2) and (c) E-field enhancement ($|E/E_0|$) spectra, for a NPoM resonator presenting the modified picopatch in (a) and otherwise the same geometry as in Figure 1c. The field enhancement is obtained at the center of the slot, and the colormaps show the dependence of the spectra on r_{slot}. The resonant wavelength of the NPoM nanocavity eigenmodes (which are independent of r_{slot}), are indicated by horizontal dashed lines in the color maps. The theoretical evolution of the uncoupled s'_{01} picopatch mode with r_{slot} (given by Equations (2) and (4)) is indicated by the diagonal dashed line in the color maps. (d) Sketch (not to scale) of the picopatch region of a resonator, showing (rotationally symmetric) regions marked with reddish color where the permittivity of Au is changed through the loss factor f, following Equation (7). (e) Scattering and (f) electric field enhancement $|E/E_0|$ spectra as a function of the loss factor f used in this picopatch region (with increasing f corresponding to larger absorption losses), for a resonator of otherwise the same geometry as in Figure 1c ($r_{slot} = 1.435$ nm). The field enhancement is obtained at the center of the vacuum slot in the picopatch (marked by a black cross in Figure 1c). The inset in (e) shows a zoom-in view of the scattering spectra from 800 to 1000 nm. Spectra of the same system but without the picopatch (bare NPoM nanocavity) are plotted as a reference by the gray dashed line. In this case, the much weaker field enhancement is evaluated in the center of the nanogap.

absorption losses. As the increase in absorption losses is likely local, we adopt this modified permittivity only in the regions around the vacuum slot, i.e., the lifted Au monolayer that forms the slot and the 0.47 nm-thick top of the Au substrate just below (corresponding to ≈2 atomic layers), as sketched by the reddish regions in Figure 7d.

The simulated scattering spectra for increasing loss factor f are plotted in Figure 7e (solid lines). In general, the scattering spectrum depends weakly on the loss factor f, which could be expected as the effect of the presence of the picopatch was already relatively small (Figure 3a). However, the NPoM with picopatch spectra remains different from that of the reference bare NPoM nanocavity without picopatch (gray dashed line) in the spectral region around $\lambda \approx 800$–1000 nm (see zoom in inset of Figure 7e), even for strongly increased losses (e.g., $f = 8$, green line).

The effect of the increased losses is clearer in the field enhancement ($|E/E_0|$) spectra, as shown in Figure 7f. As the loss factor f is increased, $|E/E_0|$ (calculated in the center of the picopatch slot) decreases substantially over the whole spectral range. Furthermore, in the spectral region around $\lambda \approx 800$ -1000 nm, the

two peaks associated with the hybrid modes become just one as f is increased. However, the field enhancement factor remains very large for all values of f considered, several times larger than those obtained for the bare NPoM nanocavity without the picopatch (gray dashed line). Thus, we find that even when the local losses are increased to be eightfold larger than the standard value, the strong field enhancement that makes picopatches interesting for nanophotonics remains robust. Further, we show in Section S8 that a similar finding applies not only to the field enhancement at the center of the picopatch slot, but also near the center of the nanocavity.

5 | Conclusions

In summary, we have analyzed in detail the optical response of NPoM resonators containing picopatches that are formed when an atomic-thick section of atoms in a NPoM nanocavity is lifted from the top layer of the underlying metallic substrate, leaving a sub-nanometer-thick vacuum slot below. This situation was identified in recent work as a morphology that could explain flare effects in metal nanoparticle fluorescence [34]. Using classical electromagnetic calculations (justified by previous quantum atomistic calculations of infinite MIMI waveguides [33]), we show that the slot mode can be tuned over a broad wavelength range and that it hybridizes with the bare NPoM cavity modes when both modes overlap spectrally. The hybridized mode has an effective mode volume close to 1 nm^3, and induces a huge $\approx$ 2000-fold electric field enhancement. Furthermore, these fields can penetrate into the metal forming the picopatch, and thus potentially explain emission flares observed in experiments. The picopatches also affect the far-field spectra, which might open an alternative path to detect their formation. Last, we illustrate how these general results are robust to changes in the picopatch shape or quantum-induced (non-local) increases of absorption losses. Thus, this study shows that the presence of picopatches in nanoresonators is a promising configuration to achieve extreme field localization and enhancement in nanophotonics.

Acknowledgements

We thank Philippe Lalanne for his help with the quasi-normal mode formalism. We acknowledge grant PID2022-139579NB-I00 funded by MICIU/AEI/10.13039/501100011033 and by ERDF, EU, and Grant Number IT 1526-22 from the Department of Science, Universities and Innovation of the Basque Government. J. H. and Y. Z. acknowledge funding from grants 17704208, 62475242 funded by National Natural Science Foundation of China, grant 2024YFE0105200 from National Key R&D Program of China, grant 252300420342 funded by Natural Science Foundation of Henan Province. X. A. acknowledges Spanish Ministerio de Ciencia, Innovación y Universidades for his PhD Grant Number FPU21/02963.

Conflicts of Interest

The authors declare no conflicts of interest.

Data Availability Statement

The data that support the findings of this study is openly available in https://digital.csic.es/handle/10261/439849.

References

1. E. Hutter and J. H. Fendler, "Exploitation of Localized Surface Plasmon Resonance," *Advanced Materials* 16 (2004): 1685–1706, https://doi.org/10.1002/adma.200400271.

2. D. K. Gramotnev and S. I. Bozhevolnyi, "Plasmonics Beyond the Diffraction Limit," *Nature Photonics* 4 (2010): 83–91, https://doi.org/10.1038/nphoton.2009.282.

3. N. J. Halas, S. Lal, W.-S. Chang, S. Link, and P. Nordlander, "Plasmons in Strongly Coupled Metallic Nanostructures," *Chemical Reviews* 111, no. 6 (2011): 3913–3961, https://doi.org/10.1021/cr200061k.

4. J. J. Mock, M. Barbic, D. R. Smith, D. A. Schultz, and S. Schultz, "Shape Effects in Plasmon Resonance of Individual Colloidal Silver Nanoparticles," *The Journal of Chemical Physics* 116 (2002): 6755–6759, https://doi.org/10.1063/1.1462610.

5. K. L. Kelly, E. Coronado, L. L. Zhao, and G. C. Schatz, "The Optical Properties of Metal Nanoparticles: The Influence of Size, Shape, and Dielectric Environment," *The Journal of Physical Chemistry B* 107, no. 3 (2003): 668–677, https://doi.org/10.1021/jp026731y.

6. L. J. Sherry, R. Jin, C. A. Mirkin, G. C. Schatz, and R. P. Van Duyne, "Localized Surface Plasmon Resonance Spectroscopy of Single Silver Triangular Nanoprisms," *Nano Letters* 6, no. 9 (2006): 2060–2065, https://doi.org/10.1021/nl061286u.

7. M. A. Garcia, "Surface Plasmons in Metallic Nanoparticles: Fundamentals and Applications," *Journal of Physics D: Applied Physics* 44 (2011): 283001, https://doi.org/10.1088/0022-3727/44/28/283001.

8. H. Xu, J. Aizpurua, M. Kall, et al., "Electromagnetic Contributions to Single-Molecule Sensitivity in Surface-Enhanced Raman Scattering," *Physical Review E* 62 (2000): 4318–4324.

9. E. Hao and G. C. Schatz, "Electromagnetic Fields Around Silver Nanoparticles and Dimers," *Journal of Chemical Physics* 120 (2004): 357–366.

10. S. Tian, J. Wang, S. Sun, et al., "Strong Field Enhancement and Hot Spot Manipulation Based on Anapole state in Si Disk-Ring Metasurfaces," *Results in Physics* 49 (2023): 106485.

11. C. Ciraci, R. T. Hill, J. J. Mock, et al., "Probing the Ultimate Limits of Plasmonic Enhancement," *Science* 337 (2012): 1072–1074.

12. G. Lévêque and O. J. F. Martin, "Optical Interactions in a Plasmonic Particle Coupled to a Metallic Film," *Optics Express* 14, no. 21 (2006): 9971–9981.

13. P. Nordlander and F. Le, "Plasmonic Structure and Electromagnetic Field Enhancements in the Metallic Nanoparticle-Film System," *Applied Physics B* 84 (2006): 35–41.

14. J. J. Mock, R. T. Hill, A. Degiron, et al., "Distance-Dependent Plasmon Resonant Coupling Between a Gold Nanoparticle and Gold Film," *Nano Letters* 8, no. 8 (2008): 2245–2252.

15. J. J. Baumberg, J. Aizpurua, M. H. Mikkelsen, and D. R. Smith, "Extreme Nanophotonics From Ultrathin Metallic Gaps," *Nature Materials* 18 (2019): 668–678, https://doi.org/10.1038/s41563-019-0290-y.

16. J. Mertens, A. L. Eiden, D. O. Sigle, et al., "Controlling Subnanometer Gaps in Plasmonic Dimers Using Graphene," *Nano Letters* 13, no. 11 (2013): 5033–5038, https://doi.org/10.1021/nl4018463.

17. S. Huang, T. Ming, Y. Lin, et al., "Ultrasmall Mode Volumes in Plasmonic Cavities of Nanoparticle-On-Mirror Structures," *Small* 12, no. 37 (2016): 5190–5199, https://doi.org/10.1002/smll.201601318.

18. Y. Li, W. Chen, X. He, et al., "Boosting Light–Matter Interactions in Plasmonic Nanogaps," *Advanced Materials* 5 (2024): 2405186, https://doi.org/10.1002/adma.202405186.

19. R. Esteban, G. Aguirregabiria, A. G. Borisov, et al., "The Morphology of Narrow Gaps Modifies the Plasmonic Response," *ACS Photonics* 2, no. 2 (2015): 295–305, https://doi.org/10.1021/ph5004016.

20. C. Tserkezis, R. Esteban, D. O. Sigle, et al., "Hybridization of Plasmonic Antenna and Cavity Modes: Extreme Optics of Nanoparticle-on-Mirror Nanogaps," *Physical Review A* 92, no. 5 (2015): 053811, https://doi.org/10.1103/PhysRevA.92.053811.

21. R. Chikkaraddy, X. Zheng, F. Benz, et al., "How Ultranarrow Gap Symmetries Control Plasmonic Nanocavity Modes: From Cubes to Spheres in the Nanoparticle-on-Mirror," *ACS Photonics* 4 (2017): 469–475, https://doi.org/10.1021/acsphotonics.6b00908.

22. M. Barbry, P. Koval, F. Marchesin, et al., "Atomistic Near-Field Nanoplasmonics: Reaching Atomic-Scale Resolution in Nanooptics," *Nano Letters* 15 (2015): 3410–3419, https://doi.org/10.1021/acs.nanolett.5b00759.

23. F. Benz, M. K. Schmidt, A. Dreismann, et al., "Single-Molecule Optomechanics in 'Picocavities," *Science* 354 (2016): 726–729.

24. C. Carnegie, J. Griffiths, B. de Nijs, et al., "Room-Temperature Optical Picocavities Below 1 nm 3 Accessing Single-Atom Geometries," *The Journal of Physical Chemistry Letters* 9, no. 24 (2018): 7146–7151, https://doi.org/10.1021/acs.jpclett.8b03466.

25. M. Urbieta, M. Barbry, Y. Zhang, et al., "Atomic-scale Lightning Rod Effect in Plasmonic Picocavities: A Classical View to a Quantum Effect," *ACS Nano* 12, no. 1 (2018): 585–595, https://doi.org/10.1021/acsnano.7b07401.

26. T. Wu, W. Yan, and P. Lalanne, "Bright Plasmons With Cubic Nanometer Mode Volumes Through Mode Hybridization," *ACS photonics* 8, no. 1 (2021): 307–314, https://doi.org/10.1021/acsphotonics.0c01569.

27. J. J. Baumberg, "Picocavities: A Primer," *Nano Letters* 22, no. 14 (2022): 5859–5865, https://doi.org/10.1021/acs.nanolett.2c01695.

28. R. Zhang, Y. Zhang, Z. C. Dong, et al., "Chemical Mapping of a Single Molecule by Plasmon-Enhanced Raman scattering," *Nature* 498 (2013): 82–86, https://doi.org/10.1038/nature12151.

29. J. Lee, K. T. Crampton, N. Tallarida, and V. A. Apkarian, "Visualizing Vibrational Normal Modes of a Single Molecule With Atomically Confined Light," *Nature* 568 (2019): 78–82, https://doi.org/10.1038/s41586-019-1059-9.

30. B. Yang, G. Chen, A. Ghafoor, et al., "Sub-Nanometre Resolution in Single-Molecule Photoluminescence Imaging," *Nature Photonics* 14, no. 11 (2020): 693–699, https://doi.org/10.1038/s41566-020-0677-y.

31. W. Li, Q. Zhou, P. Zhang, and X.-W. Chen, "Bright Optical Eigenmode of 1 nm3 Mode Volume," *Physical Review Letters* 126 (2021): 257401, https://doi.org/10.1103/PhysRevLett.126.257401.

32. B. Song, J. Jansen, F. D. Tichelaar, et al., "In-Situ Transmission Electron Microscopy and First-principles Study of Au (100) Surface Dislocation Dynamics," *Surface Science* 608 (2013): 154–164, https://doi.org/10.1016/j.susc.2012.10.003.

33. J. J. Baumberg, R. Esteban, S. Hu, et al., "Quantum Plasmonics in Sub-Atom-Thick Optical Slots," *Nano Letters* 23 (2023): 10696–10702, https://doi.org/10.1021/acs.nanolett.3c02537.

34. C. Carnegie, M. Urbieta, R. Chikkaraddy, et al., "Flickering Nanometre-Scale Disorder in a Crystal Lattice Tracked by Plasmonic Flare Light Emission," *Nature Communications* 11 (2020): 682, https://doi.org/10.1038/s41467-019-14150-w.

35. W. Chen, P. Roelli, A. Ahmed, et al., "Intrinsic Luminescence Blinking From Plasmonic Nanojunctions," *Nat Commun* 12 (2021): 2731.

36. M. M. Schmidt, E. A. Farley, M. A. Engevik, et al., "High-Speed Spectral Characterization of Single-Molecule SERS Fluctuations," *ACS nano* 17, no. 7 (2023): 6675–6686, https://doi.org/10.1021/acsnano.2c12457.

37. COMSOL Multiphysics® v. 6.0. cn.comsol.com. COMSOL AB, Stockholm, Sweden.

38. O. Stenzel, *The Physics of Thin Film Optical Spectra: An Introduction* (Springer, 2005).

39. P. B. Johnson and R. W. Christy, "Optical Constants of the Noble Metals," *Physical Review B* 6 (1972): 4370–4379, https://doi.org/10.1103/PhysRevB.6.4370.

40. S. I. Bozhevolnyi and T. Søndergaard, "General Properties of Slow-Plasmon Resonant Nanostructures: Nano-Antennas and Resonators," *Optics Express* 15 (2007): 10869, https://doi.org/10.1364/OE.15.010869.

41. J. Jung, T. Søndergaard, and S. I. Bozhevolnyi, "Gap Plasmon-Polariton Nanoresonators: Scattering Enhancement and Launching of Surface Plasmon Polaritons," *Physical Review B* 79 (2009): 035401, https://doi.org/10.1103/PhysRevB.79.035401.

42. R. Esteban, T. V. Teperik, and J. J. Greffet, "Optical Patch Antennas for Single Photon Emission Using Surface Plasmon Resonances," *Physical Review Letters* 104, no. 2 (2010): 026802, https://doi.org/10.1103/PhysRevLett.104.026802.

43. M. Kuttge, F. J. García de Abajo, and A. Polman, "Ultrasmall Mode Volume Plasmonic Nanodisk Resonators," *Nano Letters* 10 (2010): 1537–1541, https://doi.org/10.1021/nl902546r.

44. J. B. Lassiter, F. McGuire, J. J. Mock, et al., "Plasmonic Waveguide Modes of Film-Coupled Metallic Nanocubes," *Nano Letters* 13 (2013): 5866–5872, https://doi.org/10.1021/nl402660s.

45. F. Minkowski, F. Wang, A. Chakrabarty, and Q. H. Wei, "Resonant Cavity Modes of Circular Plasmonic Patch Nanoantennas," *Applied Physics Letters* 104 (2014): 021111, https://doi.org/10.1063/1.4862430.

46. J. A. Dionne, L. A. Sweatlock, H. A. Atwater, and A. Polman, "Plasmon Slot Waveguides: Towards Chip-Scale Propagation With Subwavelength-Scale Localization," *Physical Review B* 73 (2006): 035407, https://doi.org/10.1103/PhysRevB.73.035407.

47. Y. Kurokawa and H. T. Miyazaki, "Metal-Insulator-Metal Plasmon Nanocavities: Analysis of Optical Properties," *Physical Review B* 75 (2007): 035411, https://doi.org/10.1103/PhysRevB.75.035411.

48. V. M. Silkin, A. García-Lekue, J. M. Pitarke, E. V. Chulkov, E. Zaremba, and P. M. Echenique, "Novel Low-Energy Collective Excitation at Metal Surfaces," *Europhysics Letters (EPL)* 66, no. 2 (2004): 260–264, https://doi.org/10.1209/epl/i2003-10184-1.

49. B. Diaconescu, K. Pohl, L. Vattuone, et al., "Low-Energy Acoustic Plasmons at Metal Surfaces," *Nature* 448, no. 7149 (2007): 57–59, https://doi.org/10.1038/nature05975.

50. S. J. Park and R. E. Palmer, "Acoustic Plasmon on the Au (111) Surface," *Physical Review Letters* 105, no. 1 (2010): 016801, https://doi.org/10.1103/PhysRevLett.105.016801.

51. J. García de Abajo, "Nonlocal Effects in the Plasmons of Strongly Interacting Nanoparticles, Dimers, and Waveguides," *Journal of Physical Chemistry C* 112, no. 46 (2008): 17983–17987.

52. T. V. Teperik, P. Nordlander, J. Aizpurua, and A. G. Borisov, "Robust Subnanometric Plasmon Ruler by Rescaling of the Nonlocal Optical Response," *Physical Review Letters* 110, no. 26 (2013): 263901, https://doi.org/10.1103/PhysRevLett.110.263901.

53. P. E. Stamatopoulou and C. Tserkezis, "Finite-Size and Quantum Effects in Plasmonics: Manifestations and Theoretical Modelling [Invited]," *Optical Materials Express* 12, no. 5 (2022): 1869, https://doi.org/10.1364/OME.456407.

54. A. Babaze, T. Neuman, R. Esteban, J. Aizpurua, and A. G. Borisov, "Dispersive Surface-Response Formalism to Address Nonlocality in Extreme Plasmonic Field Confinement," *Nanophotonics* 12, no. 16 (2023): 3277–3289, https://doi.org/10.1515/nanoph-2023-0178.

55. V. Gupta, J. L. Montaño-Priede, S. Hu, et al., "Emission Enhancement of Colloidal Quantum Dots Confined in Double Disc Nano-antennas With Controlled Opening," *Nanoscale* 18 (2026): 1576–1588, https://doi.org/10.1039/D5NR03524D.

56. N. Kongsuwan, A. Demetriadou, M. Horton, R. Chikkaraddy, J. J. Baumberg, and O. Hess, "Plasmonic Nanocavity Modes: From Near-Field to Far-Field Radiation," *ACS Photonics* 7, no. 2 (2020): 463–471, https://doi.org/10.1021/acsphotonics.9b01445.

57. B. Luk'yanchuk, N. I. Zheludev, S. A. Maier, et al., "The Fano Resonance in Plasmonic Nanostructures and Metamaterials," *Nature Materials* 9 (2010): 707–715, https://doi.org/10.1038/nmat2810.

58. J. He, C. Fan, P. Ding, S. Zhu, and E. Liang, "Near-Field Engineering of Fano Resonances in a Plasmonic Assembly for Maximizing CARS Enhancements," *Scientific Reports* 6 (2016): 20777, https://doi.org/10.1038/srep20777.

59. Á. Nodar, T. Neuman, Y. Zhang, J. Aizpurua, and R. Esteban, "Fano Asymmetry in Zero–Detuned Exciton–Plasmon Systems," *Optics Express* 31 (2023): 10297–10319, https://doi.org/10.1364/OE.477200.

60. L. Novotny, "Effective Wavelength Scaling for Optical Antennas," *Physical Review Letters* 98 (2007): 266802, https://doi.org/10.1103/PhysRevLett.98.266802.

61. J. Dorfmüller, R. Vogelgesang, R. T. Weitz, et al., "Fabry-Pérot Resonances in One-Dimensional Plasmonic Nanostructures," *Nano Letters* 9 (2009): 2372–2377, https://doi.org/10.1021/nl900900r.

62. R. Gordon, "Light in a Subwavelength Slit in a Metal: Propagation and Reflection," *Physical Review B* 73 (2006): 153405, https://doi.org/10.1103/PhysRevB.73.153405.

63. E. S. Barnard, J. S. White, A. Chandran, and M. L. Brongersma, "Spectral Properties of Plasmonic Resonator Antennas," *Optics Express* 16 (2008): 16529–16537, https://doi.org/10.1364/OE.16.016529.

64. J. Bellessa, C. Bonnand, J. C. Plenet, and J. Mugnier, "Strong Coupling Between Surface Plasmons and Excitons in an Organic Semiconductor," *Physical Review Letters* 93 (2004): 036404, https://doi.org/10.1103/PhysRevLett.93.036404.

65. P. Törmä and W. L. Barnes, "Strong Coupling Between Surface Plasmon Polaritons and Emitters: A Review," *Reports on Progress in Physics* 78, no. 1 (2014): 013901.

66. T. J. Antosiewicz, S. P. Apell, and T. Shegai, "Plasmon–exciton Interactions in a Core–Shell Geometry: From Enhanced Absorption to Strong Coupling," *ACS Photonics* 1 (2014): 454–463, https://doi.org/10.1021/ph500032d.

67. R. Chikkaraddy, B. de Nijs, F. Benz, et al., "Single-molecule Strong Coupling at Room Temperature in Plasmonic Nanocavities," *Nature* 535, no. 7610 (2016): 127–130, https://doi.org/10.1038/nature17974.

68. H. Leng, B. Szychowski, M.-C. Daniel, and M. Pelton, "Strong Coupling and Induced Transparency at Room Temperature With Single Quantum Dots and Gap Plasmons," *Nature Communications* 9 (2018): 4012, https://doi.org/10.1038/s41467-018-06450-4.

69. M. Autore, P. Li, I. Dolado, et al., "Boron Nitride Nanoresonators for Phonon-enhanced Molecular Vibrational Spectroscopy at the Strong Coupling Limit," *Light: Science & Applications* 7 (2018): 17172, https://doi.org/10.1038/lsa.2017.172.

70. X. Wu, S. K. Gray, and M. Pelton, "Quantum-Dot-Induced Transparency in a Nanoscale Plasmonic Resonator," *Optics Express* 18, no. 23 (2010): 23633–23645, https://doi.org/10.1364/OE.18.023633.

71. A. Babaze, R. Esteban, A. G. Borisov, and J. Aizpurua, "Electronic Exciton–Plasmon Coupling in a Nanocavity Beyond the Electromagnetic Interaction Picture," *Nano Letters* 21 (2021): 8466–8473, https://doi.org/10.1021/acs.nanolett.1c03202.

72. U. Muniain, J. Aizpurua, R. Hillenbrand, L. Martín-Moreno, and R. Esteban, "Description of Ultrastrong Light–Matter Interaction Through Coupled Harmonic Oscillator Models and their Connection With Cavity-QED Hamiltonians," *Nanophotonics* 14 (2025): 2031–2052, https://doi.org/10.1515/nanoph-2024-0528.

73. G. Khitrova, H. M. Gibbs, M. Kira, S. W. Koch, and A. Scherer, "Vacuum Rabi Splitting in Semiconductors," *Nature Physics* 2, no. 2 (2006): 81–90, https://doi.org/10.1038/nphys227.

74. E. Prodan, C. Radloff, N. J. Halas, and P. Nordlander, "A Hybridization Model for the Plasmon Response of Complex Nanostructures," *Science* 302, no. 5644 (2003): 419–422, https://doi.org/10.1126/science.1089171.

75. E. Prodan and P. Nordlander, "Plasmon Hybridization in Spherical Nanoparticles," *The Journal of Chemical Physics* 120, no. 11 (2004): 5444–5454, https://doi.org/10.1063/1.1647518.

76. W. Chen, S. Zhang, M. Kang, et al., "Probing the Limits of Plasmonic Enhancement Using a Two- Dimensional Atomic Crystal Probe," *Light: Science & Applications* 7 (2018): 56, https://doi.org/10.1038/s41377-018-0056-3.

77. Z. Lu, J. Ji, H. Ye, H. Zhang, S. Zhang, and H. Xu, "Quantifying the Ultimate Limit of Plasmonic Near-Field Enhancement," *Nature Communications* 15 (2024): 8803, https://doi.org/10.1038/s41467-024-53210-8.

78. E. M. Purcell, "Spontaneous Emission Probabilities at Radio Frequencies," *Physical Review* 69 (1946): 681.

79. J. T. Robinson, C. Manolatou, L. Chen, and M. Lipson, "Ultrasmall Mode Volumes in Dielectric Optical Microcavities," *Physical Review Letters* 95, no. 14 (2005): 143901, https://doi.org/10.1103/PhysRevLett.95.143901.

80. R. Esteban, J. Aizpurua, and G. W. Bryant, "Strong Coupling of Single Emitters Interacting With Phononic Infrared Antennae," *New Journal of Physics* 16, no. 1 (2014): 013052, https://doi.org/10.1088/1367-2630/16/1/013052.

81. A. F. Koenderink, "On the Use of Purcell Factors for Plasmon Antennas," *Optics Letters* 35, no. 24 (2010): 4208–4210, https://doi.org/10.1364/OL.35.004208.

82. C. Sauvan, J. P. Hugonin, I. S. Maksymov, and P. Lalanne, "Theory of the Spontaneous Optical Emission of Nanosize Photonic and Plasmon Resonators," *Physical Review Letters* 110 (2013): 237401, https://doi.org/10.1103/PhysRevLett.110.237401.

83. P. T. Kristensen and S. Hughes, "Modes and Mode Volumes of Leaky Optical Cavities and Plasmonic Nanoresonators," *ACS Photonics* 1, no. 1 (2014): 2–10, https://doi.org/10.1021/ph400114e.

84. J. Sepulveda, J. L. Montaño-Priede, J. Aizpurua, and R. Esteban, "Semianalytical Treatment of Collective Vibrational Strong Coupling in Infrared Phononic and Plasmonic Nanoantennas," *The Journal of Physical Chemistry C* 129 (2025): 12374–12390, https://doi.org/10.1021/acs.jpcc.5c00458.

85. P. Lalanne, W. Yan, K. Vynck, C. Sauvan, and J.-P. Hugonin, "Light Interaction With Photonic and Plasmonic Resonances," *Laser & Photonics Reviews* 12 (2018): 1700113, https://doi.org/10.1002/lpor.201700113.

86. W. Yan, R. Faggiani, and P. Lalanne, "Rigorous Modal Analysis of Plasmonic Nanoresonators," *Physical Review B* 97, no. 20 (2018): 205422, https://doi.org/10.1103/PhysRevB.97.205422.

87. S. Franke, S. Hughes, M. K. Dezfouli, et al., "Quantization of Quasinormal Modes for Open Cavities and Plasmonic Cavity Quantum Electrodynamics," *Physical Review Letters* 122 (2019): 213901, https://doi.org/10.1103/PhysRevLett.122.213901.

88. T. Wu, M. Gurioli, and P. Lalanne, "Nanoscale Light Confinement: The Q's and V's," *ACS Photonics* 8, no. 6: 1522–1538, https://doi.org/10.1021/acsphotonics.1c00336.

89. J. M. Lourtioz, H. Benisty, V. Berger, and J. M. Gérard, *Photonic Crystals: Towards Nanoscale Photonic Devices* (Springer, 2005).

90. M. Aspelmeyer, T. J. Kippenberg, and F. Marquardt, *Cavity Optomechanics: Nano- and Micromechanical Resonators Interacting With Light* (Springer, 2014), https://doi.org/10.1007/978-3-642-55312-7.

91. J. M. Gerard and B. Gayral, "Strong Purcell Effect for InAs Quantum Boxes in Three-Dimensional Solid-State Microcavities," *Journal of Lightwave Technology* 17 (1999): 2089–2095, https://doi.org/10.1109/50.802999.

92. Z. Huang, X. Lin, Z. Lu, et al., "Identifying High-Order Plasmon Modes in Silver Nanoparticle-Over-Mirror Configuration," *Optics Express* 32, no. 11 (2024): 19746–19756, https://doi.org/10.1364/OE.522105.

Supporting Information

Additional supporting information can be found online in the Supporting Information section.

Supporting File: lpor71540-sup-0001-SuppMat.docx.